



# Suppression of repeated adiabatic shear banding by dynamic large strain extrusion machining

S.L. Cai, L.H. Dai\*

State Key Laboratory of Nonlinear Mechanics, Institute of Mechanics, Chinese Academy of Sciences, Beijing 100190, China

## ARTICLE INFO

### Article history:

Received 20 July 2013

Received in revised form

29 August 2014

Accepted 4 September 2014

Available online 17 September 2014

### Keywords:

Dynamic large strain extrusion machining

High speed machining

Thermo-plastic instability

Shear band spacing

Momentum diffusion

## ABSTRACT

High speed machining (HSM) is an advanced production technology with great future potential. Chip serration or segmentation is a commonly observed phenomenon during high speed machining of metals, which is found to be ascribed to a repeated shear band formation fueled by thermo-plastic instability occurring within the primary shear zone. The occurrence of serrated chips leads to the cutting force fluctuation, decreased tool life, degradation of the surface finish and less accuracy in machine parts during high speed machining. Hence, understanding and controlling serrated chip formation in HSM are extremely important. In this work, a novel dynamic large strain extrusion machining (DLSEM) technique is developed for suppressing formation of serrated chips. The systematic DLSEM experiments of Ti–6Al–4V and Inconel 718 alloy with varying degrees of imposed extrusion constraint were carried out. It is found that there is a prominent chip morphology transition from serrated to continuous state and shear band spacing decreases with the constraint degree increasing. In order to uncover underlying mechanism of the imposed extrusion constraint suppressing repeated adiabatic shear banding in DLSEM, new theoretical models are developed where the effects of extrusion constraint, material convection due to chip flow and momentum diffusion during shear band propagation are included. The analytical expressions for the onset criterion of adiabatic shear band and shear band spacing in DLSEM are obtained. The theoretical predictions are in agreement with the experimental results.

© 2014 Elsevier Ltd. All rights reserved.

## 1. Introduction

High speed machining (HSM) has become an important development area in advanced manufacturing technology due to the enhanced manufacturing efficiency and much improved product quality. More recently, theoretical and experimental investigations have been performed to study the feasibility of HSM (Burns and Davies, 1997, 2002; Molinari et al., 2002, 2013; Ye et al., 2013). A universal phenomenon is found during these investigations, that is to say, with increasing cutting velocity, the continuous smooth chip flow breaks down and serrated chips begin to form. Especially for the difficult-to-cut materials such as Ti–6Al–4V and Inconel 718 alloy, the serrated chips are more prone to appear with increasing cutting speed (Burns and Davies, 2002; Molinari et al., 2002; Schulz and Moriwaki, 1992; Ye et al., 2013). The occurrence of serrated

\* Corresponding author. Tel.: +86 10 82543958; fax: +86 10 82543977.

E-mail address: [lhcai@lnm.imech.ac.cn](mailto:lhcai@lnm.imech.ac.cn) (L.H. Dai).

chips leads to the cutting force fluctuation, decreased tool life, degradation of the surface finish and less accuracy in machine parts (Atlati et al., 2011; Davies et al., 1996). Therefore, the formation of serrated chip should be avoided during HSM in technology.

In science, the serrated chip formation is originated from the repeated thermo-plastic shear banding within primary shear zone (PSZ) in HSM, which has been demonstrated in more and more works (Burns and Davies, 2002; Molinari et al., 2002, 2013; Recht, 1964, 1985; Ye et al., 2012, 2013). The mechanism of multiple shear bands in HSM is different from that in simple shear because the materials convection exists in the former. The detailed discussions on multiple shear banding in simple shear can be found in several books and reviews (Bai and Dodd, 1992; Batra and Wei, 2006; Dodd and Bai, 2012; Grady and Kipp, 1987; Meyers, 1994; Meyers et al., 2001; Molinari, 1997; Wright, 2002; Wright and Ockendon, 1996; Xue et al., 2002, 2004; Zhang and Clifton, 2003; Zhou et al., 1996a, 1996b). As for the multiple shear bands in serrated chips during machining, Huang and Aifantis put forward a laconic method to predict the shear band spacing in serrated chip formation by multiplying the chip flow speed by the characteristic instability time (Huang and Aifantis, 1997, 2007). Molinari and co-workers assumed that segment spacing was related to the characteristic perturbation wave length for which the corresponding perturbation grown rate reached a maximum (Molinari, 1997; Molinari et al., 2013, 2002). The scaling laws in serrated chip formation were obtained in their numerical and dimensional analysis. Meyers and co-workers made a systematic experimental study and found that in many cases the shear band spacing was different at different loading stages (Meyers et al., 2001; Xue et al., 2002, 2004). In order to consider the later stage of shear localization, Ye et al. not only considered the momentum diffusion and material convection (due to chip flow), but also took into account the shear band evolution in the prediction of segment spacing for serrated chip formation (Ye et al., 2013).

The previous works are concerned about serrated chip formation and shear band spacing in serrated chip during free machining (FM). The studies have demonstrated that the state of stress in PSZ has a significant effect on the chip formation in FM, so a constraint is introduced into PSZ to change the state of stress and shear banding evolution in this paper. Actually, Chiffre first put forward extrusion-cutting to impose the extrusion stress in PSZ for changing the chip formation (De Chiffre, 1976). Recently, Chandrasekar and co-workers devised a large strain extrusion machining (LSEM) apparatus to fabricate ultrafine grain materials (UFG) at a low cutting speed (Brown et al., 2009; Efe et al., 2012). However, the research on the effect of extrusion on chip flow stability or adiabatic shear banding in HSM is vacant. Inspired by the works of Chiffre and Chandrasekar, we developed a novel dynamic large strain extrusion machining (DLSEM) device based on split Hopkinson pressure bar (SHPB) to explore effect of extrusion on the formation of adiabatic shear bands or serrated chips in HSM. By making use of the DLSEM device, a systematic DLSEM experiments for difficult-to-cut materials (e.g. Ti–6Al–4V and Inconel 718 alloy) with different constraint effects were made in this paper. The shear band morphology and segment chip spacing were examined for different constraint levels. It is found that the imposed extrusion plays a significant role in suppressing the emergence of thermo-plastic shear bands or serrated chips during DLSEM. To elucidate the mechanisms of the suppression on repeated thermo-plastic shear banding during DLSEM, the theoretical models for onset of adiabatic shear band and the multiple shear band spacing are established, where the momentum diffusion, thermal diffusion, material convection induced by the rapid chip flow, and the extrusion of constraint are included. The explicit expressions for the onset criterion of adiabatic shear band in DLSEM and the shear band spacing are derived. The analytical results are in agreement with the experimental observations, and the underlying physics and dynamic evolution of adiabatic shear bands in DLSEM are clearly revealed.

The paper is organized as follows: in Section 2 we briefly narrate the experimental procedure of the DLSEM Ti–6Al–4V and Inconel 718 alloy. The experimental observations of shear band morphology and shear band spacing are given in Section 3. Section 4 presents the analytical models for the onset of shear instability and shear band spacing in detail. The discussions on underlying physics of shear bands in DLSEM are made in Section 4. Section 5 gives remarkable conclusions of our present investigation.

## 2. Experimental procedure

The sample materials used in the experiments are Ti–6Al–4V and Inconel 718 alloy with chemical composition specified in Table 1. The annealing temperatures of Ti–6Al–4V and Inconel 718 alloy are 700–785 °C and 927 °C, respectively. The mechanical properties of Ti–6Al–4V and Inconel 718 alloy are listed in Table 2. The samples were taken from the bar material and the microstructures of three section planes in the workpiece are shown in Fig. 1.

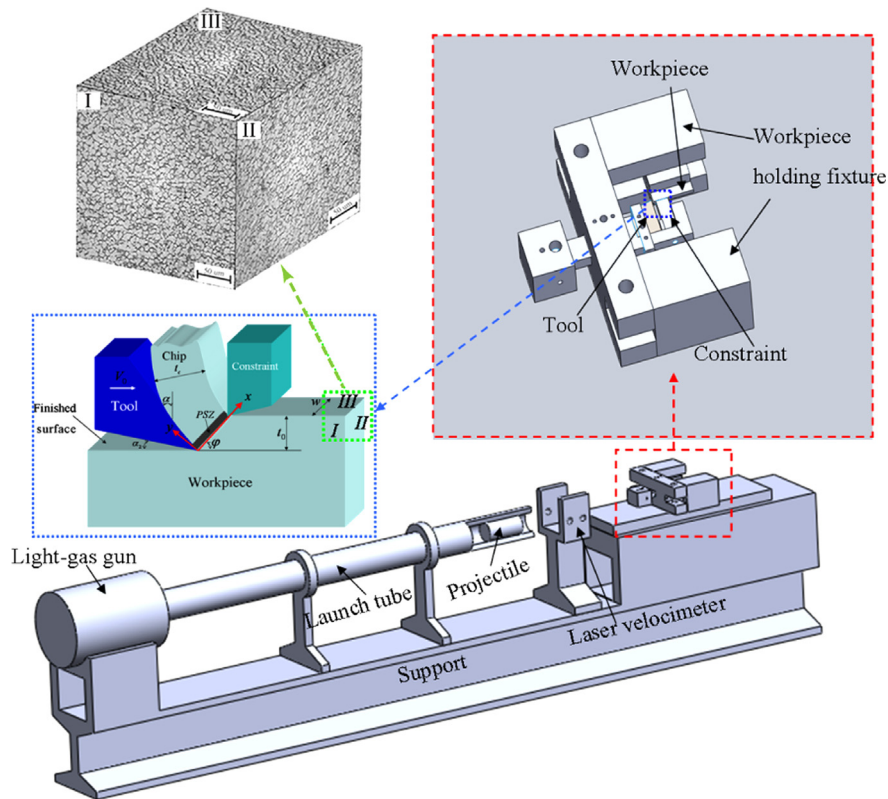
**Table 1**  
Chemical composition of Ti–6Al–4V and Inconel 718 alloy.

Ti–6Al–4V	Elements wt(%)	Ti 87.73–91	Al 5.5–6.75	V 3.5–4.5	Fe 0.4	C 0.08	N 0.03	H 0.015	O 0.2
Inconel 718	Elements wt(%)	Ni 50–55	Cr 17–21	Fe 19	Nb 4.75–5.5	Mo 2.8–3.3	Ti 0.65–1.15	Al 0.3–0.7	Others ≤ 0.81

**Table 2**

Mechanical properties and parameters for Ti-6Al-4V and Inconel 718 alloy.

Properties and parameters	Notation	Ti-6Al-4V	Inconel 718
Density	$\rho$ (kg m <sup>-3</sup> )	4430	8190
Elastic modulus	$E$ (GPa)	110	205
Thermal conductivity	$k$ (W m <sup>-1</sup> K <sup>-1</sup> )	6.6	11.1
Specific heat capacity	$c$ (J kg <sup>-1</sup> K <sup>-1</sup> )	670	435
Initial yield stress	$A$ (MPa)	782.7	1029
Hardening modulus	$B$ (MPa)	498.4	1477
Strain rate dependency coefficient	$C$	0.028	0.06
Work-hardening exponent	$n$	0.28	0.33
Thermal softening exponent	$m$	1	1.44
The reference strain rate	$\dot{\epsilon}_0$ (s <sup>-1</sup> )	$1 \times 10^{-5}$	1
Ambient temperature	$T_a$ (K)	293	293
Melting temperature	$T_m$ (K)	1873	1570
Thermal softening coefficient	$\alpha_T$ (K <sup>-1</sup> )	$8 \times 10^{-4}$	$6.4 \times 10^{-4}$
Strain rate hardening coefficient	$\zeta$ (Pa s <sup>-1</sup> )	0.75	0.75

**Fig. 1.** Schematic for DLSEM processes with parameters and the microstructures of three section planes of workpiece.**Table 3**

Cutting condition in DLSEM Ti-6Al-4V and Inconel 718 alloy.

Cutting parameters	Notation	Ti-6Al-4V			Inconel 718
Rake angle	$\alpha$	0°			0°
Clearance angle	$\alpha_2$	5°			5°
Precut chip thickness	$t_0$ (μm)	100			100
Cutting width	$w$ (mm)	2			2
Cutting speed	$V_0$ (m/s)	5	10	15	10
Controlled chip thickness	$t_c$ (μm)	80–170	30–170	30–170	70–240
Chip compression ratio	$\psi$	0.8–1.7	0.3–1.7	0.3–1.7	0.7–2.4
Constraint extrusion factor	$\chi$	0–0.53	0–0.82	0–0.82	0–0.71



Fig. 1 shows a schematic of the DLSEM which is conducted on split Hopkinson pressure bar (SHPB). The chip thickness  $t_c$  is controlled by the constraint in DLSEM. Here, we consider an orthogonal machining process, where a wedge-shaped tool with a rake angle  $\alpha$  is moving toward the workpiece with a precut depth  $t_0$  at the cutting speed  $V_0$ . Based on the definition of chip compression ratio (CCR)  $\psi = t_c/t_0$  (Astakhov and Shvets, 2004; Astakhov and Xiao, 2008), the different CCRs are

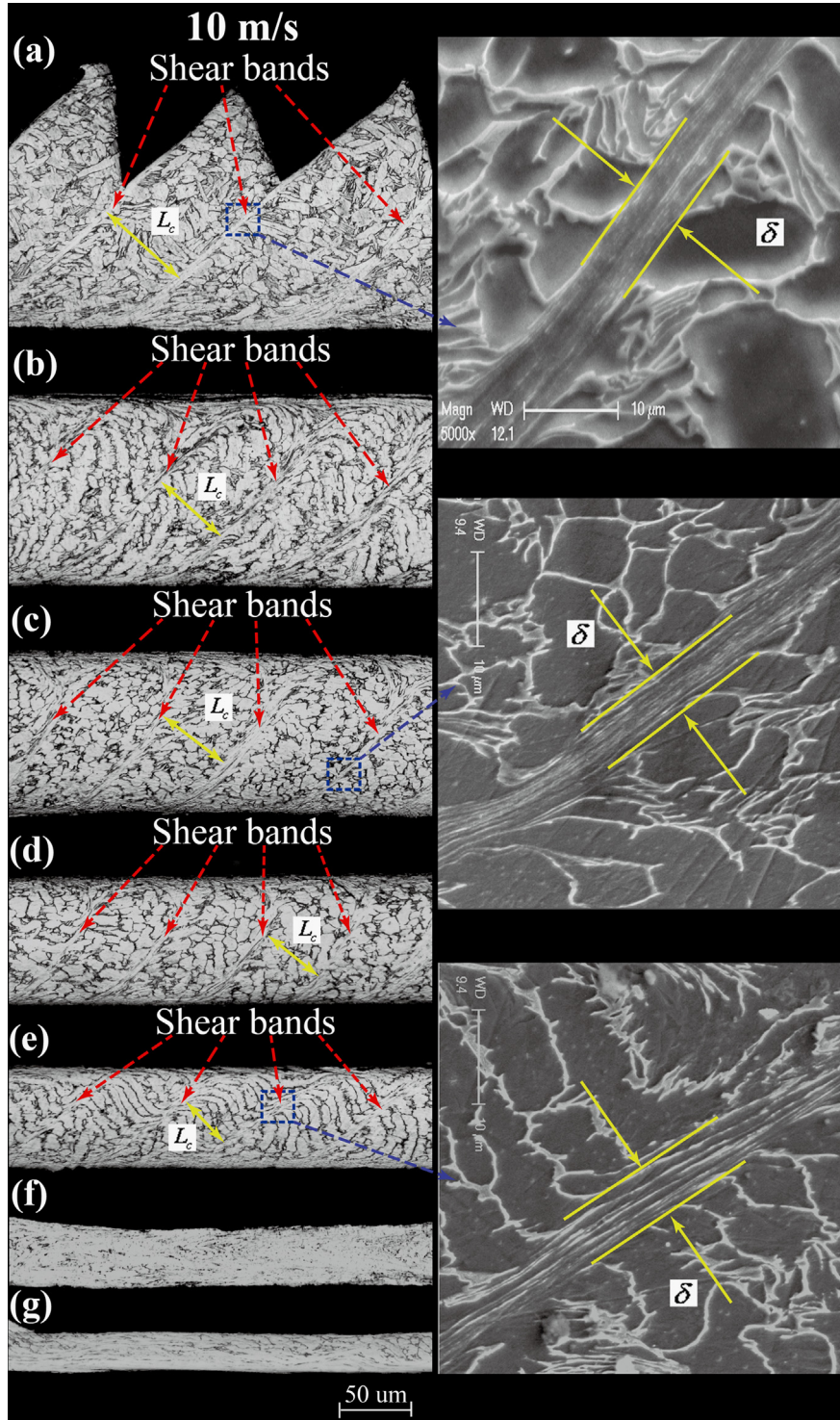


**Fig. 2.** The transition from shear band like localized deformation to homogeneous deformation with increasing CEF at the cutting speed of 10 m/s in DLSEM Ti6Al4V: (a) CEF=0 (FM); (b) CEF=0.18; (c) CEF=0.35; (d) CEF=0.47; (e) CEF=0.59; (f) CEF=0.71; and (g) CEF=0.82.

obtained by changing the position of constraint in the experiments. The maximum of CCR  $\psi$  is the corresponding CCR  $\psi_F$  for FM (i.e.  $\psi \leq \psi_F$ ). To characterize the constraint extrusion effect, the constraint extrusion factor (CEF)  $\chi$  is introduced and can be defined as  $\chi = (\psi_F - \psi) / \psi_F$  ( $\chi \in (0, 1)$ ). It is found that the constraint may have an increasing influence on chip formation in DLSEM with  $\chi$  increasing. For  $\chi = 0$ , it corresponds to FM where the constraint is not imposed. In order to explore the relationship between different CEFs and shear instability during DLSEM difficult-to-cut materials, the different cutting conditions for DLSEM Ti-6Al-4V and Inconel 718 alloy are listed in Table 3. By adjusting the position of constraint, the required CEFs can be realized, which are listed in Table 3. After cutting, chips were collected and embedded into clean resin. The lateral process was mechanically polished and then the polished surfaces were etched in the different etching solutions to reveal the deformed microstructure of Ti-6Al-4V and Inconel 718 alloy (e.g. a 2%HF+4%HNO<sub>3</sub>+94%H<sub>2</sub>O solution lasting for 10 s for Ti-6Al-4V and a 7%HNO<sub>3</sub>+13%HF+80%HCl+5gFeCl<sub>3</sub> solution lasting for 20 s for Inconel 718). These etched specimens were observed with the optical microscope (Olympus BX51M) and the scanning electron microscope (SEM FEI Sirion400NC) to examine the morphologies of chips and adiabatic shear bands.

### 3. Experimental observations

In the light of Schulz and Moriwaki, the lower and upper limits for high-speed machining of titanium alloy is about 1.5 m/s and 15 m/s respectively (Schulz and Moriwaki, 1992), and therefore, the cutting speed 10 m/s in the experiments is sufficient to produce shear bands in chips for free machining (FM). Generally, the parameters that characterize chip morphologies are the segment spacing (shear band spacing)  $L_c$  and the shear band width  $\delta$  illustrated in Fig. 2 (Molinari et al., 2002; Schulz et al., 2001). Fig. 2a and Fig. 2b–g correspond to FM and DLSEM respectively. As for FM, the chips are serrated due to the absence of extrusion constraint and the shear bands are obviously observed between the saw-teeth like chips. However, in the condition of DLSEM, the chips become continuous and the suppression by the imposed constraint on adiabatic shear banding in chips can clearly be seen from Fig. 2b–g. When CEF reaches or exceeds a critical value, i.e.  $\chi = 0.71$ , the thermo-plastic shear instability is totally suppressed and adiabatic shear bands disappear in chips (see in Fig. 2f–g). In this case, homogeneous plastic deformation is realized in chips. From the magnified figures marked in Fig. 2, several features should be noticed. First, the microstructure outside the shear band is greatly different from that inside for both FM and DLSEM: the grains inside the shear bands are elongated along the shear direction and have undergone an extremely large deformation, while those outside shear bands almost remain the same with undeformed structures. Second, the width of shear bands in DLSEM is nearly equal to that in FM at the same cutting speed 10 m/s. In addition, for FM case where the extrusion constraint vanishes, the shear bands evolve fully and the grains in FM refine more severely than those in DLSEM.

Moreover, the microstructure evolutions with different CEFs in DLSEM are illustrated in Fig. 2 in which Fig. 2a–g comes from chips obtained for the CEF of 0 (FM), 0.18, 0.35, 0.47, 0.59, 0.71 and 0.82 respectively at the cutting speed of 10 m/s. All measurements of segment spacing (shear band spacing)  $L_c$  for different CEFs were carried out for at least 10 neighboring segments and the average-weighted segment spacing was regarded as the segment spacing for each situation. It is obvious that the constraint makes three roles in the DLSEM process. First, the constraint may change the morphology of chips. The chips in FM are serrated (Fig. 2a) but those in DLSEM are continuous (Fig. 2b–g). Second, the constraint has a distinct effect on suppressing the occurrence of the shear bands. When the CEF exceeds a specific value, namely 0.71, shear bands could not emerge and the deformation in chips is homogeneous as seen in Fig. 3f and g. However, the shear bands can be produced in chips when CEF is below the specific value as shown in Fig. 2a–e. Third, the constraint could control the evolution of shear bands. As for FM, the shear bands evolve completely and the chips are serrated significantly. With CEF increasing, the constraint effect becomes more significant leading to a great resistance to shear band evolution (see in

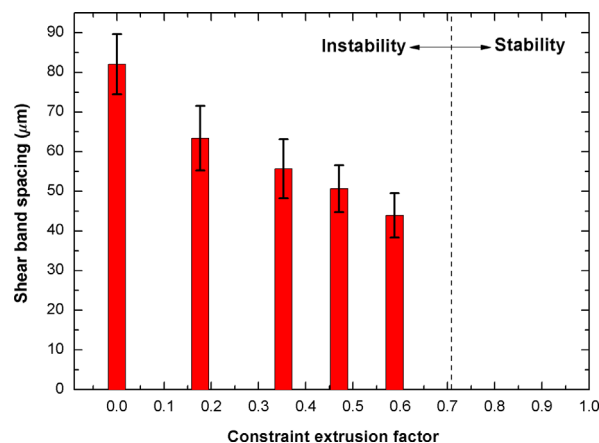


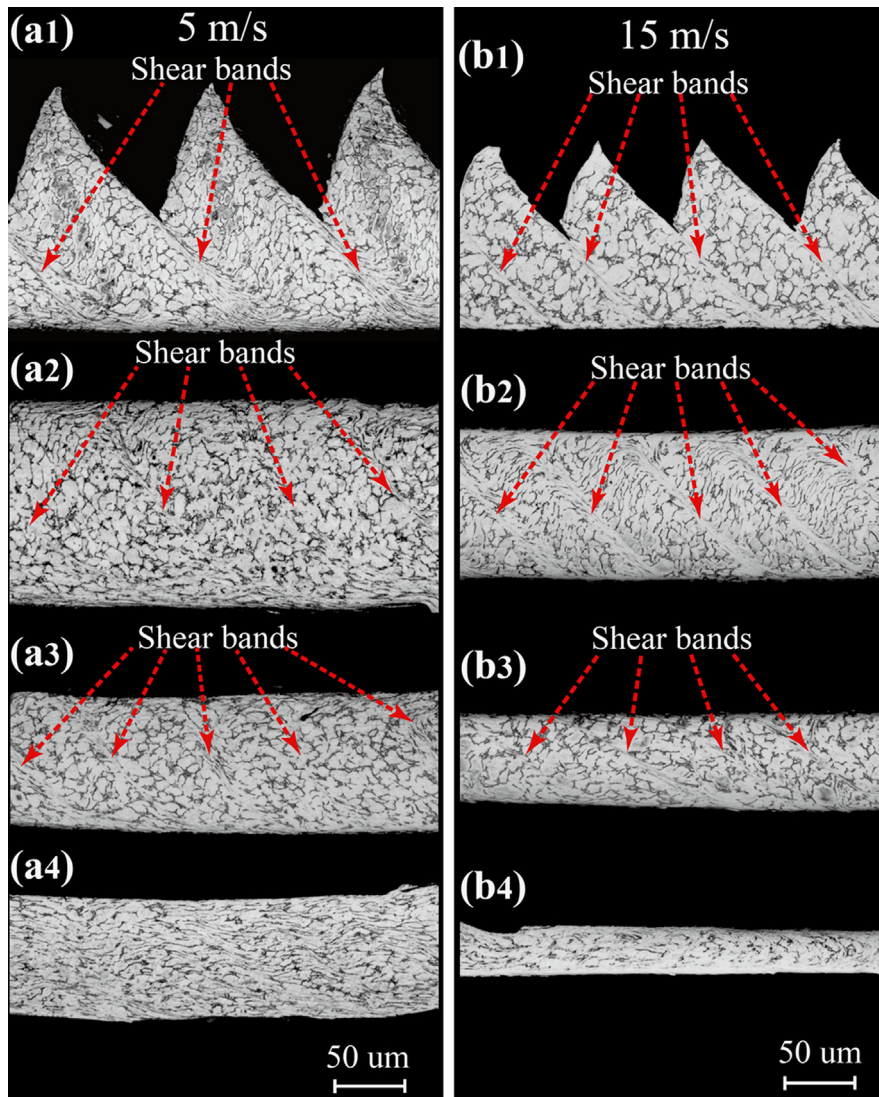
Fig. 3. The statistic shear band spacing in DLSEM Ti6Al4V at the cutting speed of 10 m/s.



Fig. 2b–e). The previous works have demonstrated that the shear band spacing increases as the shear band evolves (Meyers et al., 2001; Xue et al., 2002, 2004; Ye et al., 2013; Zhou et al., 2006a, 2006b). Therefore, the shear band spacing decreases with CEF increasing, our experimental results are in coincidence with this prediction.

The statistical shear band spacing for each CEF is illustrated in Fig. 3. The CEF of 0.71 is an important line of demarcation to distinguish stability from instability. The chip deformation is stable above the CEF of 0.71, but the chip deformation becomes unstable under that CEF. As for the instability in chips, the shear band spacing decreases with the CEF increasing shown in Fig. 3.

In order to study what a role the strain rate makes during DLSEM, the other two different cutting speeds (5 m/s and 15 m/s) were chosen to conduct the experiments in DLSEM Ti–6Al–4V for different CEFs (see in Table 3). The microstructure evolutions with different CEFs are illustrated in Figs. 4, and a1–a4 come from chips obtained for the CEF of 0, 0.12, 0.41 and 0.53 respectively at the cutting speed of 5 m/s, and b1, b2, b3 and b4 correspond to the CEF of 0, 0.35, 0.59 and 0.82 respectively at the cutting speed of 15 m/s. The transition from shear band like localized deformation to homogeneous deformation with increasing CEF is independent of the cutting speed; however, the critical CEF distinguishing instability from stability depends on the cutting speed. For low strain rate (5 m/s), the shear bands disappear in chips when CEF reaches the value of 0.53; however, for high strain rate (15 m/s), the shear bands still exist in chips for the CEF of 0.59. Moreover, the larger CEF (0.82 in Fig. 4b1) is required for restraining the shear instability at the speed of 15 m/s. The critical CEF increases with the increasing cutting speed.



**Fig. 4.** Microstructure of chips obtained for different CEFs at different cutting speeds in DLSEM Ti6Al4V: a1–a4 corresponding to the CEF of 0 (FM), 0.12, 0.41 and 0.53 respectively at the cutting speed of 5 m/s; b1–b4 corresponding to the CEF of 0 (FM), 0.35, 0.59 and 0.82 respectively at the cutting speed of 15 m/s.

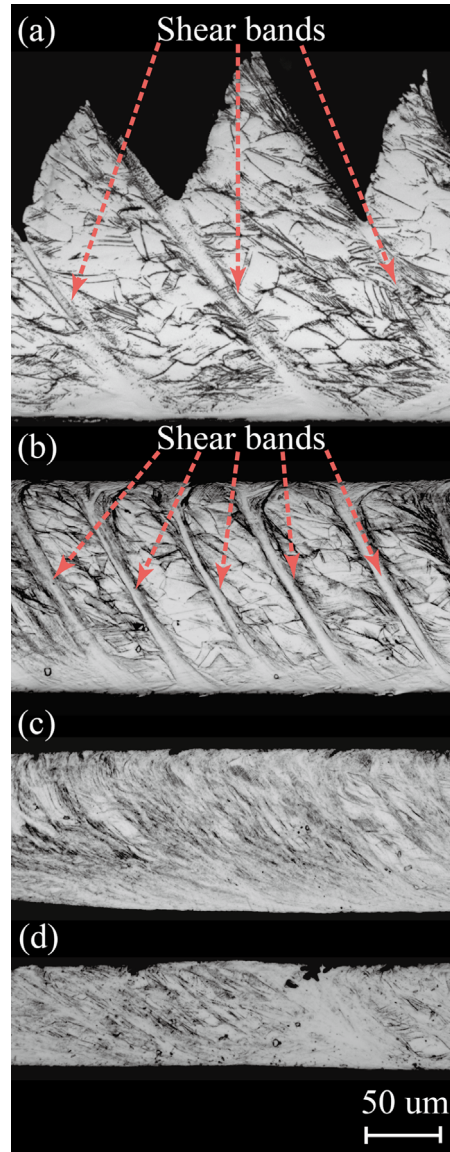


**Fig. 5.** The transition from shear band like localized deformation to homogeneous deformation with increasing CEF at the cutting speed of 10 m/s in DLSEM Inconel 718: (a) CEF=0 (FM); (b) CEF=0.38; (c) CEF=0.54; and (d) CEF=0.71.

In order to testify if the suppressing of shear banding instability in DLSEM is in force for other alloys, the DLSEM experiments on another difficult-to-machine material nickel superalloy Inconel 718 were also conducted under the cutting condition in Table 3. As shown in Fig. 5, the transition from shear band type localized deformation to homogeneous deformation can also be observed, but the critical CEF is different from that of Ti6Al4V alloy. The shear deformation is localized for free machining and it becomes homogeneous when CEF exceeds a certain value (0.54). The critical CEF of Inconel 718 alloy is smaller than that of Ti6Al4V alloy.

#### 4. Theoretical modeling for DLSEM

##### 4.1. The governing equations

Fig. 6 shows a schematic of the DLSEM, in which the free machining (FM) is marked by the dashed lines. The wedge-shaped tool with a rake angle  $\alpha$  is static, and the workpiece with a precut depth  $t_0$  is moving toward the tool at the cutting speed  $V_0$  and then flows out along the rake face of the tool in the form of a chip with a controlled chip thickness  $t_c$  at the speed  $V_c$ . In the FM case (a controlled chip thickness  $170\ \mu\text{m}$  in experiments), the constraint does not affect the chip formation and the thickness of chip formed is  $t_c^*$ . The deformation of the workpiece ahead of the tool concentrates within

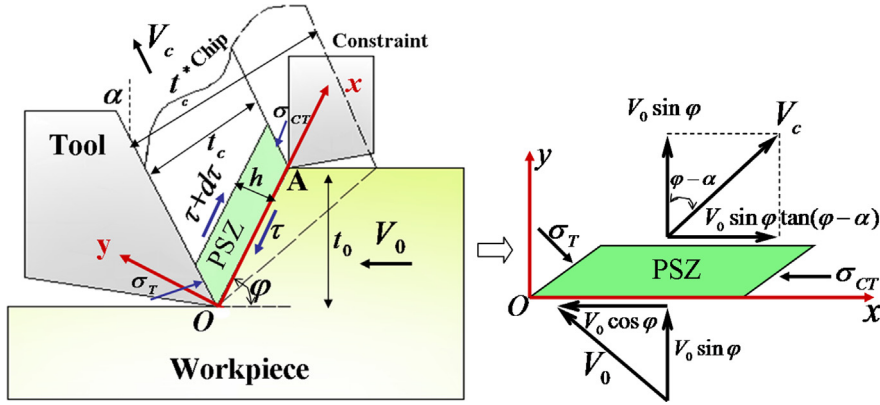


Fig. 6. The schematic of the DLSEM model, in which FM is marked by the dashed lines.

the primary shear zone (PSZ) of a finite width  $h$ . The PSZ is assumed to be parallel-sided (Hill, 1954a, 1954b; Oxley, 1989; Piispanen, 1948; Shaw, 2005). An Eulerian coordinate system ( $xoy$ ) is attached to the static tool with the  $x$ -axis parallel to the direction of shear flow and the  $y$ -axis normal to the direction respectively shown in Fig. 6. The workpiece is considered to be thermo-viscoplastic material, and its constitutive equation is given by  $\tau = f(\gamma, \dot{\gamma}, T)$ , where  $\gamma$  is the shear strain,  $\dot{\gamma}$  is the shear strain rate, and  $T$  is the temperature. For later use, let us introduce the following notations as did by Bai (1982):  $Q = (\partial f / \partial \gamma) > 0$  (strain hardening coefficient),  $R = (\partial f / \partial \dot{\gamma}) > 0$  (strain hardening coefficient) and  $P = -(\partial f / \partial T) > 0$  (thermal softening coefficient).

According to the velocity vector relationships given by Merchant and Shaw (Merchant, 1945; Shaw, 1950), the chips flow speed along the rake face of the tool is expressed as

$$V_c = \frac{V_0 \sin \varphi}{\cos(\varphi - \alpha)}, \quad (1)$$

where the shear angle  $\varphi$  is given by De Chiffre (1976)

$$\tan(\varphi - \alpha) = \frac{1}{\mu \cos \alpha} - \tan \alpha. \quad (2)$$

The cutting speed  $V_0$  and the chip speed  $V_c$  are resolved into two components parallel and normal to the direction of shear flow respectively, and then the velocity  $V(x, y, t)$  at  $y = 0$  and  $y = h$  in the PSZ shown in Fig. 6 are given by

$$\begin{cases} V_x(x, 0, t) = -V_0 \cos \varphi; V_y(x, 0, t) = V_0 \sin \varphi \\ V_x(x, h, t) = V_0 \sin \varphi \tan(\varphi - \alpha); V_y(x, h, t) = V_0 \sin \varphi \end{cases} \quad (3)$$

In the current analysis, the deformation can only occur in the  $x$  direction but may have a gradient in the  $y$  direction. Therefore, the velocity component  $V_x(x, y, t)$  and  $V_y(x, y, t)$  are only a function of the coordinate  $y$  and the time  $t$ , namely  $V_x(x, y, t) = V(y, t)$  and  $V_y(x, y, t) = V^*(y, t)$ . For the deformation in machining, a further assumption is made: the speed perpendicular to PSZ ( $y$  direction) is a constant. Combined with Eq. (3), the velocity component  $V^*(y, t)$  is equal to  $V_0 \sin \varphi$ . Then, the deformation can be formulated in a one-dimensional framework; the variables  $\tau, \gamma, \dot{\gamma}, T$  depend solely on coordinate  $y$  and time  $t$ .

The momentum is conserved in PSZ during DLSEM, so the momentum equation is given by

$$\frac{\partial^2 \tau}{\partial y^2} + \xi \frac{\partial \sigma_T}{\partial y} - \eta \frac{\partial \sigma_{CT}}{\partial y} = \rho \left( \frac{\partial \dot{\gamma}}{\partial t} + V_0 \sin \varphi \frac{\partial \dot{\gamma}}{\partial y} \right), \quad (4)$$

where  $\sigma_T$  is the compressive stress from the rake tool face,  $\sigma_{CT}$  is the compressive stress from the constraint, and  $\rho V_0 \sin \varphi \frac{\partial \dot{\gamma}}{\partial y}$  is the change of momentum due to material convection resulted from chip flow. In the equation,  $\rho$ ,  $c$ , and  $k$  are material parameters (density, specific heat capacity and thermal conductivity respectively).  $\xi$  and  $\eta$  are the geometric parameters:  $\xi = \sin \varphi (1 + \mu \tan(\alpha - \varphi)) / t_0$ ,  $\eta = \sin \varphi / t_0 \cos(\alpha - \varphi)$  where  $\mu$  is the frictional coefficient between the rake tool face and chips.  $\xi$  is introduced into the momentum equation by Burns and Davies for taking the tool compressive stress into consideration (Burns and Davies, 2002), and  $\eta$  is added into the momentum equation due to considering the constraint. As for FM,  $\eta$  is not included in Eq. (4) and Eq. (4) is the same as the momentum equation of Burns and Davies (2002). Compared with the momentum equation in simple shear (Dodd and Bai, 2012; Meyers, 1994; Walley, 2007; Wright, 2002), the effect of the compressive stresses from the tool and the constraint as well as material convection due to chips flow are added in Eq. (4) during DLSEM. The tool compressive stress  $\sigma_T$  can be written as (Burns and Davies, 1997)

$$\sigma_T = \frac{E \sin \varphi}{t_0} \int_0^t [V_s - V(y, t)] dt, \quad (5)$$



where  $V_s = V_0 \cos \alpha / \cos(\varphi - \alpha)$  is the shear speed in PSZ (Merchant, 1945; Shaw, 1950) and  $E$  is the elastic modulus of the workpiece material. The following relationship can be obtained from Eq. (5):

$$\frac{\partial^2 \sigma_T}{\partial t \partial y} + V_0 \sin \varphi \frac{\partial^2 \sigma_T}{\partial y^2} = -\frac{E \sin \varphi}{t_0} \dot{\gamma}. \quad (6)$$

Here, inspired by the work of Burns and Davies (1997), we assume that the constraint compressive stress  $\sigma_{CT}$  from constraint is given by

$$\sigma_{CT} = E \frac{t_T \cdot V(y, t)}{t_c^*}, \quad (7)$$

where  $t_T = t_c^* - t_c / V_s$  is the average time of constraint in the DLSEM process. Based on the definition of CEF, the constraint compressive stress  $\sigma_{CT}$  is written by  $\sigma_{CT} = \bar{\sigma}(V(y, t) / V_s)$  where  $\bar{\sigma} = E\chi$ . As for FM,  $t_c^*$  is equal to  $t_c$  and the constraint compressive stress  $\sigma_{CT}$  is zero. For DLSEM, the constraint compressive stress increases with CEF increasing. By making a partial derivative of Eq. (7) with respect to  $y$ , the relationship between  $\sigma_{CT}$  and  $\dot{\gamma}$  is obtained:

$$\frac{\partial \sigma_{CT}}{\partial y} = \frac{\bar{\sigma}}{V_s} \dot{\gamma}. \quad (8)$$

The conservation equation of energy is written in the following form:

$$\frac{\partial T}{\partial t} = \frac{\beta \tau}{\rho c} \dot{\gamma} + \frac{k}{\rho c} \frac{\partial^2 T}{\partial y^2} - V_0 \sin \varphi \frac{\partial T}{\partial y}, \quad (9)$$

where  $\beta$  is Taylor–Quinney coefficient. Eq. (9) states that there are three different physical processes altering the temperature in PSZ: heat generation due to plastic working (the first term in the right side of the equation), diffusion and mass transfer of heat (the second and third terms, respectively). It is noted that the mass transfer of heat is due to the material moving outwards PSZ (see Fig. 6), which should be important during the DLSEM process.

The compatibility equation is

$$\dot{\gamma} = \frac{\partial V(y, t)}{\partial y} = \frac{\partial \gamma}{\partial t} + V_0 \sin \varphi \frac{\partial \gamma}{\partial y}, \quad (10)$$

where  $V_0 \sin \varphi$  is the velocity of materials moving perpendicular to PSZ.

The initial condition (IC) and the boundary condition (BC) governing the one-dimensional DLSEM are given by

$$IC \begin{cases} \gamma(y, 0) = 0 \\ \dot{\gamma}(y, 0) = \frac{V_s}{h} \\ T(y, 0) = T_a \end{cases}, \quad (11)$$

where  $T_a$  is the ambient temperature and

$$BC \begin{cases} V(0, t) = -V_0 \cos \varphi \\ V(h, t) = V_0 \sin \varphi \tan(\varphi - \alpha) \end{cases}. \quad (12)$$

If the specific form of constitutive relation is given, we can solve simultaneously the coupled governing Eqs. (4), (6) and (8)–(12) for PSZ of shear stress, shear strain, shear strain rate and temperature in course of DLSEM.

#### 4.2. Homogeneous deformation solution

According to Jiang and Dai (2009), the deformation within a shear band can be approximately regarded as a highly localized homogeneous deformation. Therefore, it is necessary to seek the homogeneous solutions by assuming that shear strain and shear strain rate are uniformly distributed within the PSZ. Meanwhile, the velocity along  $x$  direction  $V(y, t)$  in PSZ is assumed to change from  $-V_0 \cos \varphi$  on the lower boundary to  $V_0 \sin \varphi \tan(\varphi - \alpha)$  on the upper boundary linearly without discontinuities. That is

$$V(y, t) = (V_s/h)y - V_0 \cos \varphi, \quad (0 \leq y \leq h). \quad (13)$$

The workpiece material is assumed to be rigid-perfectly plastic for simplicity and the Johnson–Cook (J–C) law was chosen to be the constitutive law of the workpiece material, which can be represented by the following formula (Johnson and Cook, 1983):

$$\tau = \frac{1}{\sqrt{3}} \left[ A + B \left( \frac{\gamma}{\sqrt{3}} \right)^n \right] \left[ 1 + C \ln \left( \frac{\dot{\gamma}}{\sqrt{3} \dot{\epsilon}_0} \right) \right] \left[ 1 - \left( \frac{T - T_a}{T_m - T_a} \right)^m \right], \quad (14)$$

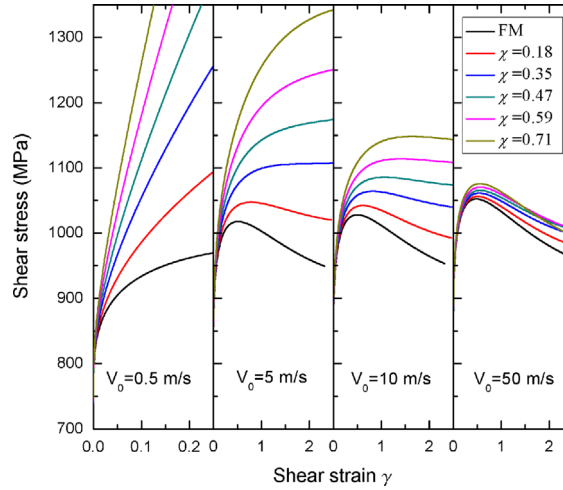


Fig. 7. The stress–strain relations for different CEFs at different cutting speeds in DLSEM: the cutting speed ranges from 0.5 to 50 m/s.

where the J–C parameter of Ti6Al4V is listed in Table 2 (Lee and Lin, 1998) and that of Inconel 718 is referred to the literature (Muthu et al., 2012). Substituting Eqs. (13) and (14) into Eqs. (4), (6), (8)–(10), then the governing equations become

$$\begin{cases} \frac{\partial^2 \tau}{\partial y^2} = \frac{E\xi}{t_0} \frac{\sin \varphi}{h} t + \frac{\eta \bar{\sigma}}{h} \\ \frac{\partial T}{\partial t} = \frac{\beta \tau}{\rho c} \frac{V_s}{h} + \frac{k}{\rho c} \frac{\partial^2 T}{\partial y^2} - V_0 \sin \varphi \frac{\partial T}{\partial y} \\ \tau = \frac{1}{\sqrt{3}} \left[ A + B \left( \frac{V_s}{\sqrt{3} \dot{\epsilon}_0 h} \right)^n \right] \left[ 1 + C \ln \left( \frac{V_s}{\sqrt{3} \dot{\epsilon}_0 h} \right) \right] \left[ 1 - \left( \frac{T - T_a}{T_m - T_a} \right)^m \right] \end{cases} \quad (15)$$

Using the finite difference method, the nonlinear partial differential equation (15) is solved for different CEF cases. The stress–strain relations of different CEFs at different cutting speeds are shown in Fig. 7.

As seen in Fig. 7, both the cutting speed and the degree of constraint have a significant effect on the shear deformation in DLSEM. The shear deformation is stable at low cutting speed (for example  $V_0 = 0.5$  m/s); however, the shear deformation is more prone to become unstable with cutting speed increasing. The constraint could suppress the thermo-plastic shear instability in DLSEM; as seen at the cutting speed of 5 m/s, the shear deformation is unstable in FM but it becomes stable for a certain degree of constraint. At relatively higher cutting speed (10 m/s), a much larger degree of constraint is needed to make the shear deformation stable. At much higher cutting speed, the shear deformation is always unstable for all of the degrees of constraint; however, the history of deformation at each CEF is different from each other. The discrepancy between the deformations of different CEFs could become smaller with the cutting speed increasing. For example, at the cutting speed of 10 m/s close to that of experiments, the shear deformation is unstable for FM (CEF=0) and the shear instability becomes more difficult with CEF increasing, which is consistent with the experiments shown in Fig. 2. For later use, we can calculate the parameters  $\tau_0$ ,  $\gamma_0$ ,  $\dot{\gamma}_0$ ,  $T_0$ ,  $Q_0$ ,  $R_0$  and  $P_0$  through the stress–strain curve when the shear deformation begins to be unstable at the cutting speed of 10 m/s.

#### 4.3. Instability analysis

The physical shear localization can be related to the mathematical instability in the differential equations governing the DLSEM. According to the dealing method introduced in Bai (1982), Clifton et al. (1984), Dai and Bai (2008), Dai et al. (2004), Jiang and Dai (2009), Molinari (1997), Molinari et al. (2002), the stability analysis is simplified by seeking an inhomogeneous deformation solution with respect to small perturbations on the homogeneous solution. Such that

$$U = U_0 + U^* \exp(pt + iqy), \quad (16)$$

where  $U$  is the inhomogeneous solutions of Eqs. (4), (6) and (8)–(10),  $U_0$  is the homogeneous solutions,  $U^*$  is small constants characterizing the magnitude of the perturbation,  $q$  is the wave number and  $p$  is the rate of growth. Substituting Eq. (16) into Eqs. (4), (6) and (8)–(10) and then only considering terms of first order in  $U^*$ , the spectral equation is derived by the following form:

$$\hat{\alpha}^3 + \left[ (1+A)\hat{k}^2 + N + C \right] \hat{\alpha}^2 + \left[ A\hat{k}^4 + (1+N-B-3D)\hat{k}^2 + M + CN \right] \hat{\alpha} + \left[ (1-D-AD)\hat{k}^4 + (M-ND-CD)\hat{k}^2 + MC \right]$$

$$+i\sqrt{D}\hat{k}\left\{3\hat{\alpha}^2+\left[2(1+A)\hat{k}^2+2N+2C\right]\hat{\alpha}+\left[A\hat{k}^4+(1+N-B-D)\hat{k}^2+M+CN\right]\right\},$$

$$=0 \quad (17)$$

where the dimensionless variables are introduced by

$$\begin{cases} \hat{\alpha} = \frac{kp}{cQ_0}, & \hat{k}^2 = \frac{k^2 q^2}{\rho c^2 Q_0}, & A = \frac{cR_0}{k}, & B = \frac{\beta P_0 \tau_0}{\rho c Q_0}, & C = \frac{\beta k P_0 \dot{\gamma}_0}{\rho c^2 Q_0}, & D = \frac{\rho V_0^2 \sin^2 \varphi}{Q_0} \\ M = \frac{k^2 \xi E \sin \varphi}{\rho c^2 t_0 Q_0^2}, & N = \frac{\eta \bar{\sigma} k}{V_s \rho c Q_0} \end{cases} \quad (18)$$

Because  $p$  is a complex number,  $\hat{\alpha}$  is also a complex number and the dimensionless growth rate  $\hat{\alpha}$  is introduced by the form of  $\hat{\alpha} = a + ib$  where  $a$  and  $b$  are the real numbers. Then, the spectral equation (17) is further transformed into the following form:

$$8a^3 + 8S_1 a^2 + 2(S_1^2 - S_2)a + S_1 S_2 - S_3 = 0, \quad (19)$$

where the polynomial coefficients are defined by

$$\begin{cases} S_1 = (1+A)\hat{k}^2 + N + C \\ S_2 = A\hat{k}^4 + (1+N-B)\hat{k}^2 + M + CN \\ S_3 = \hat{k}^4 + M\hat{k}^2 + MC \end{cases} \quad (20)$$

The stability of the DLSEM process is now determined by the sign of  $a$ : if  $a < 0$ , the shear deformation in DLSEM is stable; otherwise, it is unstable. According to the mathematical analysis, if  $S_2 < 0$ , i.e.,

$$B > 1 + N + A\hat{k}^2 + \frac{M + CN}{\hat{k}^2}, \quad (21)$$

there is at least a positive real root in all roots of Eq. (19). Therefore, Eq. (21) is an onset condition of thermo-plastic shear instability in DLSEM. It is of interest to seek the easiest instability situation, and for the easiest instability mode where  $\hat{k} = \sqrt[4]{\frac{M+CN}{A}}$ , the instability condition of DLSEM is converted to

$$\frac{B}{1 + N + 2\sqrt{A(M+CN)}} > 1. \quad (22)$$

In this instability criterion (22),  $B$  represents the effect of thermal softening which causes the instability in DLSEM. When  $B$  increases, the thermal softening has an increasing influence on instability and chip flow in DLSEM is more prone to be unstable.  $A$  and  $M$  reflect the strain rate hardening and work hardening respectively, which are the resistance of instability.  $N$  represents the effect of constraint hardening which also resists the instability. It is noted that  $N$  is a distinctive feature in DLSEM comparing with conventional free machining. It can be seen that this constraint hardening effect increases with CEF  $\chi$  increasing, which provides a high resistance to shear instability. This observation is in accordance with the experiments shown in Fig. 2. For free machining ( $N = 0$ ), the instability criterion becomes  $\frac{B}{1 + 2\sqrt{AM}} > 1$ . In the condition of simple shear where  $M$  and  $N$  are both equal to zero corresponding to the thermo-plastic simple shear, the instability criterion further simplifies the form  $B > 1$  which is the same as that derived by Bai (1982). From instability criterion (22), we can analyze the phenomenon of instability in DLSEM in details by applying the homogeneous deformation results.

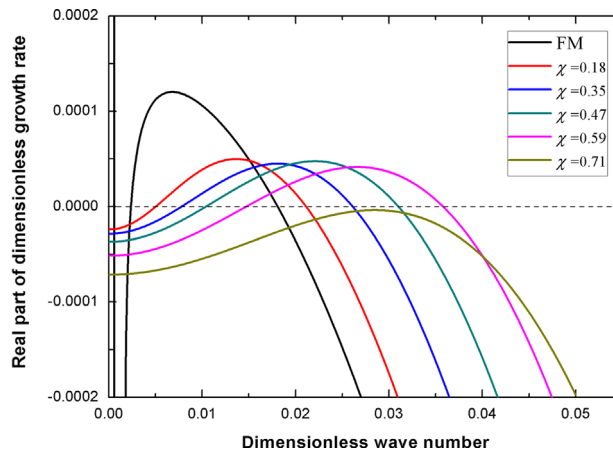


Fig. 8. Relationship between the real part of dimensionless growth rate and dimensionless wave number in the condition of the different CEFs.

By introducing the calculation results of the finite difference method for homogeneous deformation into Eq. (19), the relationship between the real part of dimensionless growth rate  $a$  and dimensionless wave number  $k$  for different CEFs at the cutting speed of 10 m/s can be shown in Fig. 8. As seen in Fig. 8, the characteristic wave number where the real part of dimensionless growth rate has a maximum increase with the CEF increasing. There will not be a positive  $a$  for all of the dimensionless wave number  $k$  if CEF exceeds a certain value of 0.71, which means that the shear deformation is stable. These analysis results are consistent with the experimental results (see in Fig. 2).

Using the homogeneous deformation solution, the variation of the instability criterion (22) from CEF at the cutting speed of 10 m/s is illustrated in Fig. 9. The stability and instability of DLSEM is separated by a specific constraint extrusion factor 0.7. If CEF is smaller than 0.7, the shear deformation is unstable; otherwise, it is stable. The prediction of instability criterion (22) is identical to the experimental results. Therefore, the instability criterion (22) is valid to predict the instability in DLSEM.

Because the instability criterion (22) is effective, it is used to determine whether the shear deformation is unstable at different cutting speeds or for different materials in DLSEM. The cutting speed takes another role in DLSEM (see in Fig. 4) and the resulting mechanical responses are different from each other at different cutting speeds. Substituting the homogeneous deformation solution (15) into the instability criterion (22), the relationship between the instability criterion value and CEF for different cutting speeds is illustrated in Fig. 10a. As seen in Fig. 10a, the theoretical model of stability analysis is still valid for different cutting speeds. The unstable shear deformation becomes stable when the CEF exceeds a certain value for different cutting speeds and the critical CEF increases with the cutting speed, which are in accordance with the experiments shown in Fig. 4. Compared with the low strain rate, the high strain rate promotes the instability and larger CEF is needed to make the shear deformation stable during DLSEM. Figs. 2 and 5 show the microstructure of chips in DLSEM different materials at the same cutting speed of 10 m/s, and it is obvious that the transition from shear band like localized deformation to homogeneous deformation with increasing CEF is material independent. By substituting homogeneous

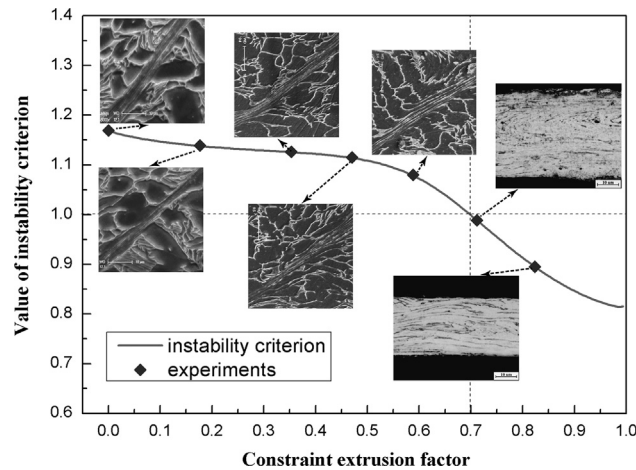


Fig. 9. Comparison of instability criterion with experimental observations at different constraint extrusion factors.

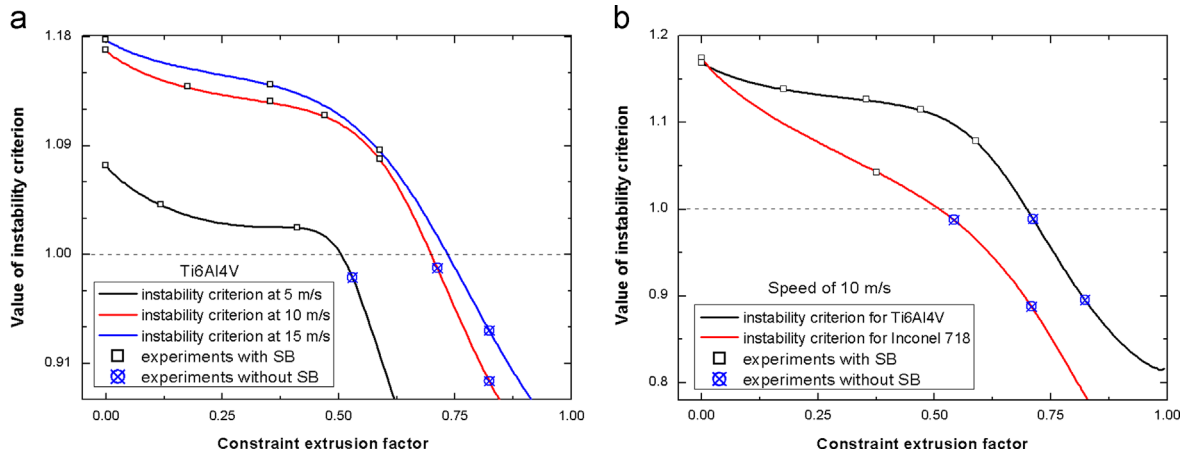


Fig. 10. (a) Relationship between the instability criterion and CEF at different cutting speeds in DLSEM Ti6Al4V; and (b) relationship between the instability criterion and CEF for Ti6Al4V and Inconel 718 at the cutting speeds of 10 m/s.



deformation solution (15) into instability criterion (22), the relationship between instability criterion value and CEF for different materials are shown in Fig. 10b. If the dimensionless number of controlling instability is above 1, the shear deformation becomes unstable; otherwise, it is stable, which is in accordance with the available experimental observations (see in Figs. 2 and 5). From Fig. 10b, the critical CEF of Inconel 718 is about 0.51 which is smaller than that of Ti6Al4V alloy (0.71). The calculated results indicate that the instability criterion is also suitable for other materials.

In order to know how the constraint may have an effect on DLSEM at different cutting speeds, the relationship between the real part of dimensionless growth rate and wave number for different CEFs at different cutting speed is obtained by introducing the calculation results of homogeneous deformation into Eq. (19). The maximum of the real part of dimensionless growth rate  $\hat{\alpha}_m$  is easily found out during the relationship between the real part of dimensionless growth rate and wave number, and then, the dimensionless instability characteristic time  $\hat{t}_m = 1/\hat{\alpha}_m$  is illustrated in Fig. 11 for different CEFs at different cutting speeds. The dimensionless instability characteristic time decreases with increasing cutting speed for different CEFs, which means that the instability of shear deformation may take place much more easily at higher cutting speed. The trend is in accordance with the available experiments during free machining titanium alloys (Arrazola et al., 2009; Gente et al., 2001; Molinari et al., 2002; Sutter and List, 2013; Ye et al., 2013). If the cutting speed is a constant, the dimensionless instability characteristic time increases with CEF increasing in DLSEM. It is revealed that the constraint may restrain the instability of thermo-plastic shear deformation in DLSEM. However, the effect that the constraint suppresses the instability becomes much smaller at higher cutting speed. It is observed in the available experiments that the morphology of chip changes from continuous to serrate during cutting titanium alloys with increasing cutting speed (Arrazola et al., 2009; Gente et al., 2001; Molinari et al., 2002; Sutter and List, 2013; Ye et al., 2013). The critical speed that makes a distinction between continuous and serrated chip is an important parameter during free machining. The solutions of homogeneous deformation at different cutting speeds are used to calculate the values of parameters in the instability condition (22), and then the values of parameters are substituted into the instability criterion (22) to determine whether the shear deformation

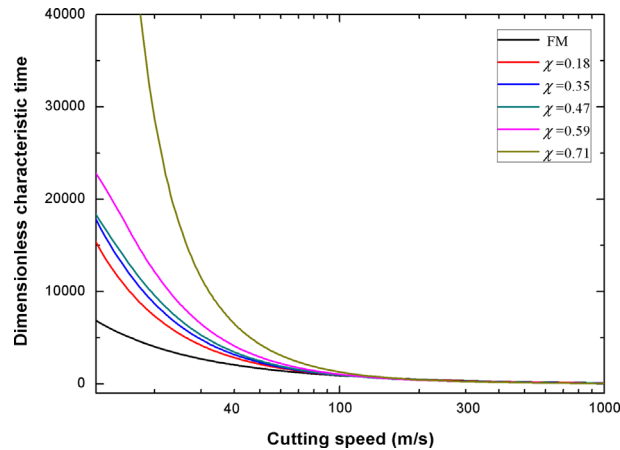


Fig. 11. Value of the dimensionless characteristic time for the CEF of 0 (FM), 0.18, 0.35, 0.47, 0.59 and 0.71 at different cutting speeds.

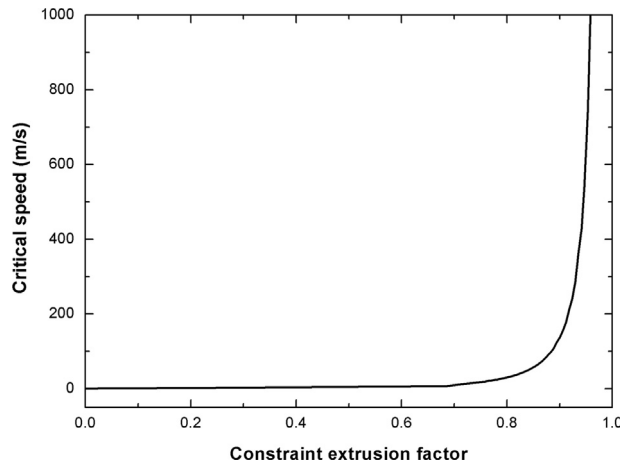


Fig. 12. Variation of critical speed with constraint extrusion factor (CEF).

in chip is stable or not. The cutting speed ranges from 0.05 m/s to 1000 m/s to find out the critical speed for different CEFs. The relationship between critical speed and CEF is shown in Fig. 12, and the critical speed is larger with CEF increasing. This is because the constraint restrains the formation of serrated chip and much higher speed is needed to promote the instability of shear deformation.

#### 4.4. Shear band spacing

When the shear deformation in PSZ is unstable, the shear bands will occur in the serrated chips. According to the mathematical instability analysis, the characteristic wave number is given by  $\hat{k} = \sqrt[4]{\frac{M+CN}{A}}$ , and the shear band spacing is obtained

$$\hat{L}_c = \frac{2\pi}{\sqrt[4]{\frac{M+CN}{A}}}. \quad (23)$$

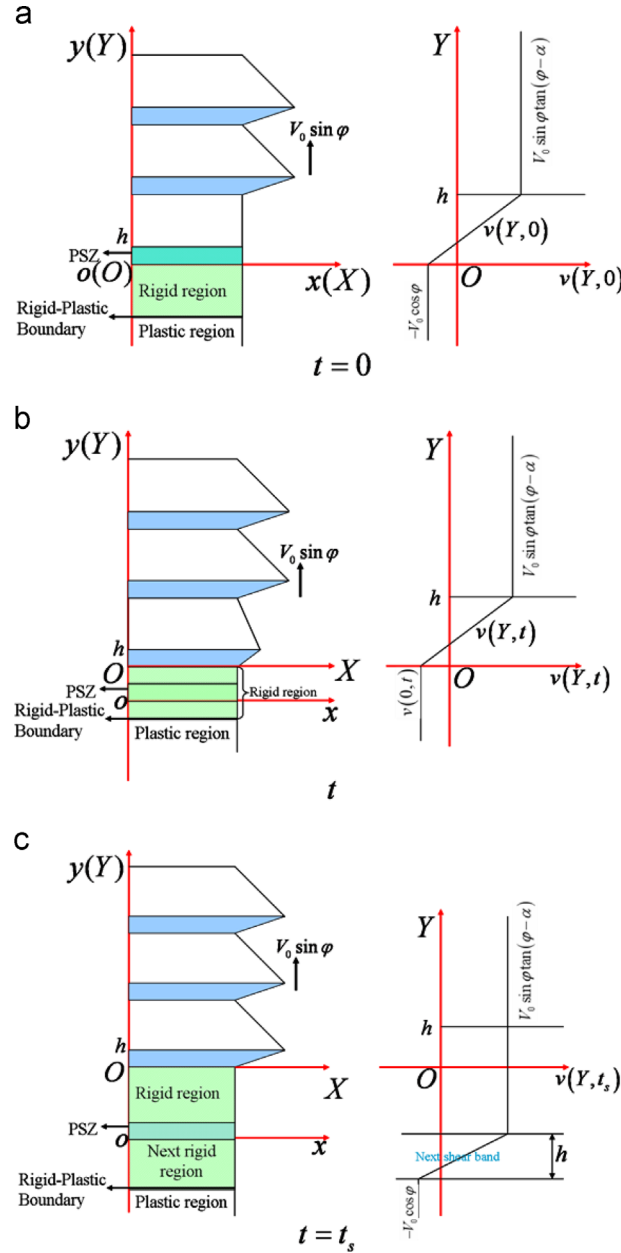


Fig. 13. (a), (b) and (c) correspond to the initial time, middle time and finished time of the shear band evolution respectively.

The shear band spacing predicted by instability analysis is much less than that of experiments in Fig. 3. As discussed by Meyers and co-workers (Meyers et al., 2001; Xue et al., 2002), the perturbation theory can make a reasonable prediction of shear band spacing at the early stage of shear band evolution. Our recent study has demonstrated that the evolution degree of shear bands has a notable effect on shear band spacing in high speed metal machining (Ye et al., 2013). The spacing at this time when the shear bands stop evolving is the shear band spacing observed in serrated chips. Therefore, the new theory for shear band spacing in DLSEM is required.

Two sets of coordinates are set up to analyze the shear band spacing in the serrated chips. The Eulerian coordinate system (xoy) is attached to the static tool with the  $x$ -axis parallel to the direction of shear flow and the  $y$ -axis normal to that direction respectively shown in Fig. 13. The Lagrangian coordinate system (XOY) is set up in chips to observe the evolution process of shear bands and moves out at the speed of  $V_0 \sin \varphi$  (seen in Fig. 13). The time when shear flow becomes unstable is chosen to be zero time. That is to say,  $t = 0$  is the time when the flow stress reached a maximum in the stress–strain curve. As shown in Fig. 13a, the Eulerian coordinate system (xoy) overlaps the Lagrangian coordinate system (XOY) at the time of  $t = 0$ . Because the Lagrangian coordinate system (XOY) flows with chips along the  $Y$  direction at the speed of  $V_0 \sin \varphi$ , the Eulerian coordinate system (xoy) is separated from the Lagrangian coordinate system (XOY) as time goes on. According to the theory of Grady, the momentum of shear bands diffuses from inside to outside as the shear bands evolve (Grady, 1992), and then a rigid unloading zone is generated. As shown in Fig. 13b, there is no shear deformation in chips when the chips move into the PSZ because of the rigid unloading zone. The shear band spacing continues to increase with the further evolution of shear bands until  $t = t_s$  when the shear band stops evolving and the next shear band starts to form (seen in Fig. 13c). The shear band spacing in serrated chips is given by multiplying the chip flow speed  $V_0 \sin \varphi$  by the time  $t_s$  for the completed evolution of one shear band. The above process is repeated all the time to produce the multiple shear bands regularly in chips.

From the speed distribution curve of  $X$ -velocity component on the right of Fig. 13a, at the time of  $t = 0$ , the speed distribution in the shear band is given by

$$\begin{cases} V(Y, 0) = -V_0 \cos \varphi, Y = 0 \\ V(Y, 0) = V_0 \sin \varphi \tan(\varphi - \alpha), Y = h \end{cases} \quad (24)$$

At the finished time of shear band evolution  $t = t_s$ , the speed distribution in shear band is obtained from the speed distribution curve of  $X$ -velocity component on the right of Fig. 13c:

$$\begin{cases} V(Y, t_s) = V_0 \sin \varphi \tan(\varphi - \alpha), Y = 0 \\ V(Y, t_s) = V_0 \sin \varphi \tan(\varphi - \alpha), Y = h \end{cases} \quad (25)$$

For  $Y = 0$ , we assume that the  $X$ -velocity component of materials is linear to the time  $t$  during the shear band evolution process. The materials above  $Y = h$  have undergone the shear band evolution process, so the  $X$ -velocity component of materials is a constant of  $V_0 \sin \varphi \tan(\varphi - \alpha)$ . The speed boundary conditions are as follows:

$$\begin{cases} V(Y, t) = \frac{V_s}{t_s} t - V_0 \cos \varphi, Y = 0 \\ V(Y, t) = V_0 \sin \varphi \tan(\varphi - \alpha), Y = h \end{cases} \quad (26)$$

It is further assumed that the  $X$ -velocity component of materials in shear band is linear to the position  $Y$  in the Lagrangian coordinate system at every time of shear band evolution:

$$V(Y, t) = \frac{V_s}{h} Y - \frac{V_s}{ht_s} Y t + \frac{V_s}{t_s} t - V_0 \cos \varphi \quad (27)$$

From Eq. (27), the relationship between the boundary displacement  $\Psi$  and time  $t$  is given by

$$\Psi = \int_0^t [V(h, t) - V(0, t)] dt = V_s t - \frac{V_s}{2t_s} t^2, \quad (28)$$

when the evolution of shear bands terminates, the boundary displacement  $\Psi_c$  is obtained

$$\Psi_c = \frac{V_s t_s}{2}. \quad (29)$$

For later analysis, the degree of shear band evolution  $\Lambda$  is introduced here in the form of  $\Lambda = \Psi / \Psi_c$ :

$$\Lambda = \frac{2}{t_s} t - \frac{1}{t_s^2} t^2, \quad (0 \leq \Lambda \leq 1). \quad (30)$$

When  $\Lambda = 0$ , it means that the shear band has just formed without evolution. If  $\Lambda = 1$ , the shear band is fully mature and the next shear band begins to form. Using the method in works of Grady (1992) and Ye et al. (2013) (Grady, 1992; Ye et al., 2013), the linear relaxation of flow shear stress is applied to approximately describe the relation of unloading stress because of shear band evolution:

$$\tau = \tau_0(1 - \Lambda), \quad (31)$$

where  $\tau_0$  is the shear stress at the moment of shear instability. Combining Eq. (30) with Eq. (31), the relationship between flow shear stress  $\tau$  and time  $t$  is achieved

$$\tau = \tau_0 \left( 1 - \frac{2}{t_s} t + \frac{1}{t_s^2} t^2 \right). \quad (32)$$

Deriving Eq. (27) with respect to  $Y$ , the shear strain rate  $\dot{\gamma}$  in shear band is given by

$$\dot{\gamma} = \frac{V_s}{h} - \frac{V_s}{ht_s} t. \quad (33)$$

For simple analysis, the constitutive relation for materials adopted by Molinari (1997) and Wright and Ockendon (1996) is used here:

$$\tau = \tau_0(1 - \alpha_T T) + \zeta \dot{\gamma}, \quad (34)$$

where  $\alpha_T$  and  $\zeta$  are the thermal softening coefficient and strain rate hardening coefficient respectively listed in Table 2. Substituting Eqs. (32) and (33) into Eq.(34), the temperature  $T$  in shear band evolution is obtained

$$T = \frac{1}{\alpha_T} \left( \frac{2}{t_s} t - \frac{1}{t_s^2} t^2 \right) + \frac{\zeta}{\tau_0 \alpha_T} \left( \frac{V_s}{h} - \frac{V_s}{ht_s} t \right). \quad (35)$$

By means of the method used by Grady (1992), the requirement of global energy consistency is imposed here by integrating the energy equation over the shear band evolution time  $t_s$ ,

$$\int_0^{t_s} \frac{dT}{dt} dt = \int_0^{t_s} \left( \frac{\tau \dot{\gamma}}{\rho c} - \frac{2k}{\rho ch^2} T \right) dt, \quad (36)$$

where  $c$  is specific heat capacity,  $k$  is thermal conductivity and  $\rho$  is density. Substituting Eqs. (32), (33) and (35) into Eq. (36), the global shear band evolution time  $t_s$  is derived by

$$t_s = \frac{1 - \alpha_T T_0}{(\tau_0 \alpha_T V_s / 4 \rho ch) - (4k / 3 \rho ch^2) - (k \zeta V_s / \rho c \tau_0 h^3)}, \quad (37)$$

where  $T_0$  is the temperature in shear band at the moment before shear instability occurs. By multiplying the chip flow speed  $V_0 \sin \varphi$  by the time  $t_s$ , the shear band spacing  $L_c$  is given by

$$L_c = \frac{(1 - \alpha_T T_0) h}{(T_\tau \alpha_T \gamma / 4) - (4V_\lambda / 3V_0 \sin \varphi) - (V_\lambda \gamma / V_\zeta)}, \quad (38)$$

where  $T_\tau = \tau_0 / \rho c$ ,  $V_\lambda = k / \rho ch$ ,  $V_\zeta = \tau_0 h / \zeta$  and  $\gamma = \frac{(1-\chi)\varphi_F}{\cos \alpha} + \frac{1}{(1-\chi)\varphi_F \cos \alpha} - 2 \tan \alpha$  respectively.

In Eq. (38),  $\alpha_T T_0$  and  $T_\tau \alpha_T$  represent the effect of thermal softening and plastic work in the process of shear band evolution respectively. The increasing  $\alpha_T T_0$  or  $T_\tau \alpha_T$  may lead to the shear band spacing increasing.  $V_\lambda$  and  $V_\zeta$  indicates the speed of thermal diffusion and strain rate hardening respectively. The shear band spacing increases with the thermal diffusion speed increasing, but it decreases with the increasing strain rate hardening speed. When the cutting speed  $V_0$  increases, the shear band spacing will decrease from Eq. (38), which is in accordance with the trend of available experiments (Molinari et al., 2002, 2013; Ye et al., 2013).  $\gamma$  in Eq. (38) reflects the influence of CEF on shear band spacing. According to the observation in experiments, the PSZ width  $h$  is chosen to be  $5 \mu\text{m}$  here because we assume that width of PSZ is equal to that

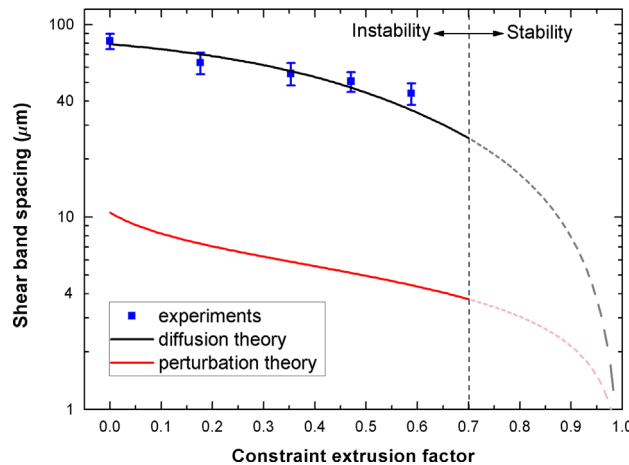


Fig. 14. Comparison of the predicted shear band spacing with the experimental observation.



of shear bands. By substituting the other parameter value into the Eqs. (23) and (38), the predicted shear band spacing of different models and experimental results of shear band spacing are shown in Fig. 14.

As shown in dotted lines in Fig. 14, the shear deformation is stable and the shear band spacing predicted by theories is useless when CEF exceeds the value of 0.7. When CEF is below the value of 0.7, the instability of shear deformation happens in PSZ and the predicted shear band spacing comes into use. According to the solid lines, the predicted shear band spacing by the present momentum diffusion theory is more consistent with the experimental results. The discussions about the difference in predicting shear band spacing between the momentum diffusion theory and the perturbation theory have been made by several researchers (Meyers et al., 2001; Xue et al., 2002, 2004); (Batra and Wei, 2006, 2007); (Molinari, 1997, 2013); (Chen et al., 2013; Ye et al., 2013).

Because Eq. (38) is effective to predict shear band spacing in DLSEM, it is also used to predict the spacing of shear bands at different cutting speeds and for different materials. The shear band spacing is calculated further at different cutting speeds or for different materials to reveal the influence from constraint in DLSEM. The variations of shear band spacing with CEF for different cutting speeds (5 m/s, 10 m/s, 15 m/s) and for different materials (Ti6Al4V and Inconel 718) are shown in Fig. 15. As seen in Fig. 15a, the predicted shear band spacing by Eq. (38) is consistent with the experimental results at different cutting speeds. The theoretical model of shear band spacing is also valid for different cutting speeds. The shear band spacing decreases with CEF increasing for a given cutting speed, and the shear deformation is stable when CEF exceeds a certain value. The extrusion effect from constraint becomes stronger with CEF increasing, leading to the degree of shear band evolution much smaller, and then the shear band spacing decreases at last. As shown in Fig. 15b, the predicted shear band spacing by Eq. (38) is consistent with the experimental results for different materials. Although the predicted shear band spacing is different from each other for the same CEF, the tendency that shear band spacing decreases with the increasing CEF remains invariable. The theoretical model of shear band spacing (38) is also valid for different materials.

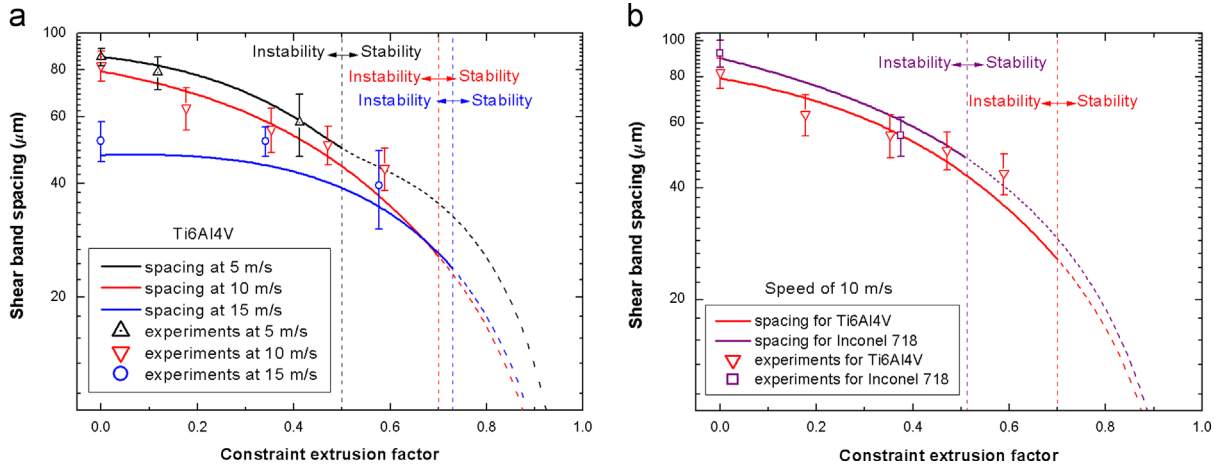


**Fig. 15.** (a) Shear band spacing varies with CEF at different cutting speeds in DLSEM Ti6Al4V; and (b) shear band spacing varies with CEF for Ti6Al4V and Inconel 718 at the cutting speeds of 10 m/s.

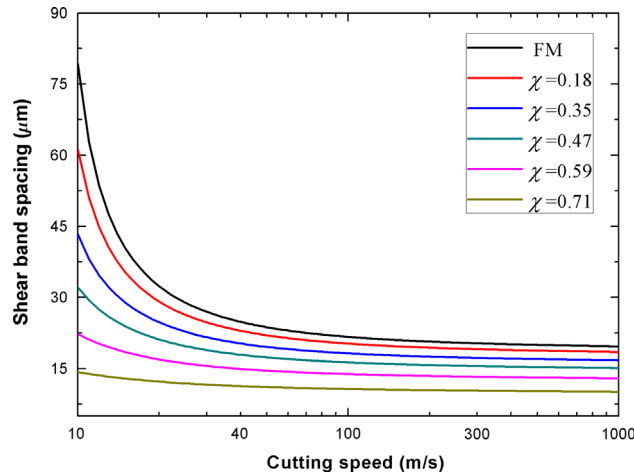


**Fig. 16.** Shear band spacing varies with cutting speed for different CEFs.

The relationship between shear band spacing and cutting speed for different CEFs is also calculated and illustrated in Fig. 16. It can be found that the larger CEF leads to smaller shear band spacing. For a given CEF, shear band spacing decreases with cutting speed increasing. The trend is in accordance with the experiments (Molinari et al., 2002; Ye et al., 2013). When the cutting speed is greater than a critical value, the shear band spacing has not much change with the cutting speed increasing (see in Fig. 16), which is in agreement with the simulation results of Molinari et al. (2013).

## 5. Concluding remarks

A novel dynamic large strain extrusion machining (DLSEM) technique is developed for suppressing formation of serrated chips. The systematic DLSEM experiments of Ti–6Al–4V and Inconel 718 alloy were undertaken for different constraint extrusion factors (CEF) at different cutting speeds. The microscopic observations of chips reveal that the transition from shear band type localized deformation to homogeneous deformation with increasing CEF is universal but the critical CEF distinguishing instability from stability depends on the cutting speed and material description; and the shear band spacing decreases with increasing CEF because the constraint suppresses the evolution of shear band. Based on the experimental observations, a theoretical model for DLSEM is developed to obtain the instability criterion and predict the shear band spacing, considering the effects of extrusion constraint, material convection due to chip flow and momentum diffusion during shear band propagation. The theoretical predictions are in agreement with the experimental results; therefore, the theoretical model is effective to predict the instability and shear band spacing in DLSEM.

## Acknowledgments

This work has been supported by the National Natural Science Foundation of China (Grant No. 11132011 and 11472287), the National Key Basic Research Program of China (Grant No. 2012CB937500) and the CAS/SAFEA International Partnership Program for Creative Research Teams.

## References

- Arrazola, P.J., Garay, A., Iriarte, L.M., Armendia, M., Marya, S., Le Maître, F., 2009. Machinability of titanium alloys (Ti6Al4V and Ti555.3). *J. Mater. Process. Technol.* 209, 2223–2230.
- Astakhov, V.P., Shvets, S., 2004. The assessment of plastic deformation in metal cutting. *J. Mater. Process. Technol.* 146, 193–202.
- Astakhov, V.P., Xiao, X.R., 2008. A methodology for practical cutting force evaluation based on the energy spent in the cutting system. *Mach. Sci. Technol.* 12, 325–347.
- Atlati, S., Haddag, B., Nouari, M., Zenasni, M., 2011. Analysis of a new Segmentation Intensity Ratio “SIR” to characterize the chip segmentation process in machining ductile metals. *Int. J. Mach. Tools Manuf.* 51, 687–700.
- Bai, Y.L., 1982. Thermo-plastic instability in simple shear. *J. Mech. Phys. Solids* 30, 195–207.
- Bai, Y.L., Dodd, B., 1992. *Adiabatic Shear Localization*. Pergamon Press, Oxford.
- Batra, R.C., Wei, Z.G., 2006. Shear band spacing in thermoviscoplastic materials. *Int. J. Impact Eng.* 32, 947–967.
- Batra, R.C., Wei, Z.G., 2007. Instability strain and shear band spacing in simple tensile/compressive deformations of thermoviscoplastic materials. *Int. J. Impact Eng.* 34, 448–463.
- Brown, T.L., Saldana, C., Murthy, T.G., Mann, J.B., Guo, Y., Allard, L.F., King, A.H., Compton, W.D., Trumble, K.P., Chandrasekar, S., 2009. A study of the interactive effects of strain, strain rate and temperature in LSEM of copper. *Acta Mater.* 57, 5491–5500.
- Burns, T.J., Davies, M.A., 1997. Nonlinear dynamics model for chip segmentation in machining. *Phys. Rev. Lett.* 79, 447–450.
- Burns, T.J., Davies, M.A., 2002. On repeated adiabatic shear band formation during high-speed machining. *Int. J. Plast.* 18, 487–506.
- Chen, Y., Jiang, M.Q., Dai, L.H., 2013. Collective evolution dynamics of multiple shear bands in bulk metallic glasses. *Int. J. Plast.* 50, 18–36.
- Clifton, R.J., Duffy, J., Hartley, K.A., Shawki, T.G., 1984. On critical conditions for shear band formation at high strain rates. *Scr. Metall.* 18, 443–448.
- Dai, L.H., Bai, Y.L., 2008. Basic mechanical behaviors and mechanics of shear banding in BMGs. *Int. J. Impact Eng.* 35, 704–716.
- Dai, L.H., Liu, L.F., Bai, Y.L., 2004. Formation of adiabatic shear band in metal matrix composites. *Int. J. Solids Struct.* 41, 5979–5993.
- Davies, M.A., Chou, Y., Evans, C.J., 1996. On chip morphology, tool wear and cutting mechanics in finish hard turning. *CIRP Ann. – Manuf. Technol.* 45, 77–82.
- De Chiffre, L., 1976. Extrusion-cutting. *Int. J. Mach. Tool Des. Res.* 16, 137–144.
- Dodd, B., Bai, Y., 2012. *Adiabatic Shear Localization*, second ed. Elsevier, Oxford.
- Efe, M., Moscoso, W., Trumble, K.P., Dale Compton, W., Chandrasekar, S., 2012. Mechanics of LSEM and application to deformation processing of magnesium alloys. *Acta Mater.* 60, 2031–2042.
- Gente, A., Hoffmeister, H.W., Evans, C.J., 2001. Chip formation in machining Ti6Al4V at extremely high cutting speeds. *CIRP Ann. – Manuf. Technol.* 50, 49–52.
- Grady, D.E., 1992. Properties of an adiabatic shear-band process zone. *J. Mech. Phys. Solids* 40, 1197–1215.
- Grady, D.E., Kipp, M.E., 1987. The growth of unstable thermoplastic shear with application to steady-wave shock compression in solids. *J. Mech. Phys. Solids* 35, 95–119.
- Hill, R., 1954a. The mechanics of machining: a new approach. *J. Mech. Phys. Solids* 2, 6.
- Hill, R., 1954b. On the limits set by plastic yielding to the intensity of singularities of stress. *J. Mech. Phys. Solids* 2, 7.
- Huang, J., Aifantis, E.C., 1997. A note on the problem of shear localization during chip formation in orthogonal machining. *J. Mater. Eng. Perform.* 6, 25–26.
- Huang, J., Aifantis, E.C., 2007. Validation of a predictive model for adiabatic shear band formation in chips produced via orthogonal machining. *J. Mech. Behav. Mater.* 18, 20.
- Jiang, M.Q., Dai, L.H., 2009. On the origin of shear banding instability in metallic glasses. *J. Mech. Phys. Solids* 57, 1267–1292.
- Johnson, G.R., Cook, W.H., 1983. A constitutive model and data for metals subjected to large strains, high strain rates and high temperatures. In: *Proceedings of the 7th International Symposium on Ballistics*, Am. Def. Prep. Ass. (ADPA), Netherlands, pp. 12–21.
- Lee, W.S., Lin, C.F., 1998. High-temperature deformation behaviour of Ti6Al4V alloy evaluated by high strain-rate compression tests. *J. Mater. Process. Technol.* 75, 127–136.
- Merchant, M.E., 1945. Mechanics of the metal cutting process. I. Orthogonal cutting and a type 2 chip. *J. Appl. Phys.* 16, 267–275.
- Meyers, M.A., 1994. *Dynamic Behavior of Materials*. Wiley, New York.

- Meyers, M.A., Nesterenko, V.F., LaSalvia, J.C., Xue, Q., 2001. Shear localization in dynamic deformation of materials: microstructural evolution and self-organization. *Mater. Sci. Eng. A* 317, 204–225.
- Molinari, A., 1997. Collective behavior and spacing of adiabatic shear bands. *J. Mech. Phys. Solids* 45, 1551–1575.
- Molinari, A., Musquar, C., Sutter, G., 2002. Adiabatic shear banding in high speed machining of Ti–6Al–4V: experiments and modeling. *Int. J. Plast.* 18, 443–459.
- Molinari, A., Soldani, X., Miguélez, M.H., 2013. Adiabatic shear banding and scaling laws in chip formation with application to cutting of Ti–6Al–4V. *J. Mech. Phys. Solids* 61, 2331–2359.
- Muthu, E., Senthamarai, K., Jayabal, S., 2012. Finite element simulation in machining of Inconel 718 nickel based superalloy. *Int. J. Adv. Eng. Appl.* 1, 5.
- Oxley, P.L.B., 1989. *Mechanics of Machining: An Analytical Approach to Assessing Machinability*. Wiley, New York.
- Piispanen, V., 1948. Theory of formation of metal chips. *J. Appl. Phys.* 19, 876–881.
- Recht, R.F., 1964. Catastrophic Thermoplastic Shear. *J. Appl. Mech.* 31, 189–193.
- Recht, R.F., 1985. A dynamic analysis of high-speed machining. *J. Eng. Ind.: Trans. ASME* 107, 309–315.
- Schulz, H., Abele, E., Sahm, A., 2001. Material aspects of chip formation in HSC machining. *CIRP Ann. – Manuf. Technol.* 50, 45–48.
- Schulz, H., Moriwaki, T., 1992. High-speed machining. *CIRP Ann. – Manuf. Technol.* 41, 637–643.
- Shaw, M.C., 1950. A quantized theory of strain hardening as applied to the cutting of metals. *J. Appl. Phys.* 21, 599–606.
- Shaw, M.C., 2005. *Metal Cutting Principles*, 2nd ed. Oxford University Press, Oxford.
- Sutter, G., List, G., 2013. Very high speed cutting of Ti–6Al–4V titanium alloy – change in morphology and mechanism of chip formation. *Int. J. Mach. Tools Manuf.* 66, 37–43.
- Walley, S.M., 2007. Shear localization: a historical overview. *Metall. Mater. Trans. A* 38A, 25.
- Wright, T.W., 2002. *The Physics and Mathematics of Adiabatic Shear Bands*. Cambridge University Press, Cambridge.
- Wright, T.W., Ockendon, H., 1996. A scaling law for the effect of inertia on the formation of adiabatic shear bands. *Int. J. Plast.* 12, 927–934.
- Xue, Q., Meyers, M.A., Nesterenko, V.F., 2002. Self-organization of shear bands in titanium and Ti–6Al–4V alloy. *Acta Mater.* 50, 575–596.
- Xue, Q., Meyers, M.A., Nesterenko, V.F., 2004. Self organization of shear bands in stainless steel. *Mater. Sci. Eng. A* 384, 35–46.
- Ye, G.G., Xue, S.F., Jiang, M.Q., Tong, X.H., Dai, L.H., 2013. Modeling periodic adiabatic shear band evolution during high speed machining Ti–6Al–4V alloy. *Int. J. Plast.* 40, 39–55.
- Ye, G.G., Xue, S.F., Ma, W., Jiang, M.Q., Ling, Z., Tong, X.H., Dai, L.H., 2012. Cutting AISI 1045 steel at very high speeds. *Int. J. Mach. Tools Manuf.* 56, 1–9.
- Zhang, Z., Clifton, R.J., 2003. Shear band propagation from a crack tip. *J. Mech. Phys. Solids* 51, 1903–1922.
- Zhou, F., Wright, T.W., Ramesh, K.T., 2006a. The formation of multiple adiabatic shear bands. *J. Mech. Phys. Solids* 54, 1376–1400.
- Zhou, F., Wright, T.W., Ramesh, K.T., 2006b. A numerical methodology for investigating the formation of adiabatic shear bands. *J. Mech. Phys. Solids* 54, 904–926.
- Zhou, M., Ravichandran, G., Rosakis, A.J., 1996a. Dynamically propagating shear bands in impact-loaded prenotched plates—II. Numerical simulations. *J. Mech. Phys. Solids* 44, 1007–1032.
- Zhou, M., Rosakis, A.J., Ravichandran, G., 1996b. Dynamically propagating shear bands in impact-loaded prenotched plates—I. Experimental investigations of temperature signatures and propagation speed. *J. Mech. Phys. Solids* 44, 981–1006.